ORIGINAL ARTICLE

lajss.org© Latin American Journal of Solids and Structures

www.lajss.org

Research on Impact Initiation of Unconfined and Confined Explosives by Explosively Formed Projectile

Guanyu Qian[a], Bin Ma[a]*

[a] School of Mechanical Engineering, Nanjing University of Science and Technology, Nanjing 210094, China.
Email: qianguangyu@njust.edu.cn, mabin@njust.edu.cn

* Corresponding author

https://doi.org/10.1590/1679-7825/e8841

Abstract

Explosively formed projectile (EFP), characterized by its insensitivity to stand-off distance and high kinetic energy, demonstrates considerable potential for application in anti-missile munitions. Numerical simulation, theoretical modeling, and experimental studies were conducted to investigate the impact initiation of both unconfined and confined explosives by EFP. A simulation model for EFP formation and its subsequent impact initiation process was developed using Autodyn software. The initiation mechanisms of explosives under varying cover plate thicknesses were analyzed, revealing a transition in the initiation mode from shock wave initiation to direct impact initiation by the residual EFP. Based on the simulation results, an equivalent diameter calculation method was proposed to characterize the impact initiation behavior of annular cross-section EFP. By integrating the A-T penetration model and the Held criterion, an engineering model for predicting the critical initiation threshold of explosives by EFP impact was established. Experimental results verify the capability of this engineering model to predict the critical cover plate thickness, as well as the accuracy of the numerical simulations.

Keywords

Explosively formed projectile; Impact initiation; Critical initiation threshold; Numerical simulation

Graphical Abstract

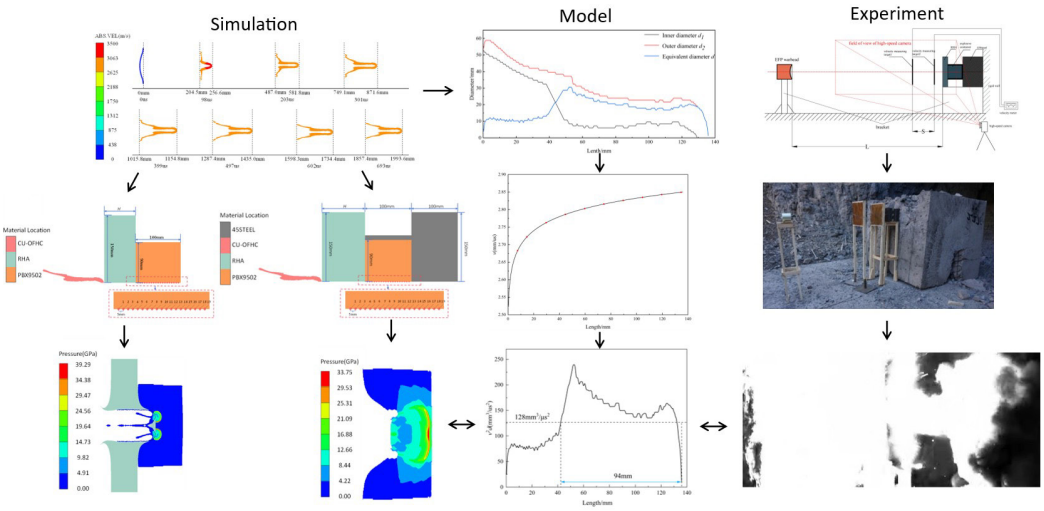

Received September 20, 2025. In revised form November 12, 2025. Accepted December 08, 2025. Available online December 10, 2025.
https://doi.org/010.1590/1679-7825/e8841

1 INTRODUCTION

Precision-guided munitions have become a key means of destroying high-value hardened targets and are playing an increasingly vital role in modern warfare. To enhance their survivability and destructive power, the warhead shell and explosive charges of such munitions are continually evolving toward thicker shell and reduced sensitivity, which poses severe challenges to traditional anti-missile munitions. To effectively intercept incoming precision-guided munitions, they must be destroyed within an extremely short time through disintegration, explosion, or detonation. Against targets with relatively thick shells, such as these, fragmentation-based interception is often ineffective. While shaped charge jet can penetrate and initiate explosives, their performance deteriorates significantly under large standoff conditions. The explosively formed projectile (EFP), formed by the inversion and closure of a liner under detonation, is characterized by its insensitivity to standoff distance and high kinetic energy. It proves effective against thick-walled targets like precision-guided munitions. Therefore, studying the impact initiation of explosives by EFP and determining the critical initiation threshold is of great significance.

Recently, many researchers have conducted several studies on the initiation of explosives using different damage elements. Regarding the critical initiation threshold, Walker and Wasley (1976) proposed the critical energy criterion $p^2\tau$ based on plate impact. James (1996) further developed the one-dimensional shock initiation research of Walker and Wasley and proposed the $Ec=p\mu\tau$ criterion. Held (1991, 1996) proposed the widely used critical initiation threshold criterion-the v^2d criterion-based on jet impact initiation experiments. Chick et al. (1986) validated the v^2d criterion using 38mm and 81mm shaped charges and proposed an initiation criterion related to jet density based on experimental results. Based on the research of Held and Chick, Chen et al. (2021, 2022) studied the critical initiation threshold of finite-thickness explosives under jet impact. Specific attention was paid to the influences of explosive thickness, shell confinement, and cover plate compression-induced desensitization effect on the critical initiation threshold, with a new theoretical model for jet impact initiation established accordingly. Zhang et al. (2006) proposed an empirical expression for the critical initiation condition on the basis of the Jacobs-Roslund empirical criterion, incorporating projectile diameter, head shape, and material parameters.

In terms of initiation mechanisms, Chick et al. (1988) investigated the initiation mechanism of bare explosives by jet impact. The study establishes that the transition from impact shock to jet bow wave initiation in bare explosives occurs at a critical ratio of the explosive's minimum detonation diameter to the jet diameter ($D/d \approx 5$). Fang et al. (1997) studied the initiation mechanisms of shelled charges, indicating that there are two primary initiation mechanisms for projectiles impacting shelled charges: shock initiation and macroscopic shear initiation. When the cover plate is thin, the initiation mechanism is shock initiation; when the cover plate is thick, the initiation mechanism involves both shock initiation and macroscopic shear initiation. Kang et al. (2022) investigated the shock initiation mechanisms of rod projectiles impacting shelled charges, proposing three initiation mechanisms: macroscopic shear initiation, low-velocity impact initiation, and high-velocity impact initiation.

Regarding EFP impact initiation of shelled charges, Li et al. (2016) conducted research on the LEFP impact initiation of high explosive anti-tank, indicating that LEFP can intercept incoming high explosive anti-tank projectiles. Guo et al. (2023) researched the shock initiation of shelled charges by single and double EFP, finding that the critical initiation cover plate thickness for dual EFP is 46.2% higher than for single EFP. Zhang et al. (2022) investigated the EFP impact initiation of column charges and obtained the influence of different impact angles on the initiation of column charges. Scholars have achieved numerous results in the field of impact initiation. However, there are no relevant reports on the initiation mechanisms of EFP on explosives or critical initiation criteria considering the shape of EFP.

In this study, the Autodyn simulation software was utilized to perform numerical simulations of the impact initiation of both unconfined and confined explosives under different cover plate thicknesses by EFP, with a focus on analyzing the initiation mechanisms of explosives at various cover plate thicknesses. Additionally, aiming at the annular cross-section of the studied EFP, a method for calculating its equivalent diameter was proposed to characterize its impact initiation behavior. On this basis, by integrating the A-T penetration model and Held's criterion, an engineering model for the critical initiation threshold of EFP impact initiation of explosives was established. Finally, experimental investigations on the impact initiation of EFP were conducted to validate the simulation results and the engineering model.

2 SIMULATION

2.1 Material model

A two-dimensional simulation model was established in Autodyn to investigate the impact initiation of explosives by an EFP. In the model, the explosive, liner, and air were modeled using Eulerian grids, while the cover plates and shell were modeled using a Lagrangian grids. The explosive was JH-2, the liner material was oxygen-free high conductivity copper (CU-OFHC), the cover plate material was Rolled Homogeneous Armor (RHA), the shell material was 45# steel, and the acceptor charge was PBX9502.

The equation of state for the PBX9502 was modeled using the Lee-Tarver model:

$$\frac{dF}{dt} = I(1-F)^b(\frac{\rho}{\rho_0} - 1 - a)^x + G_1(1-F)^c F^d P^y + G_2(1-F)^e F^g P^z \quad (1)$$

In Equation (1), *F* represents the degree of reaction of the explosive, ρ and ρ_0 denote the current and initial densities of the explosive, respectively, and *P* represents the pressure. *I*, G_1, G_2, *a*, *b*, *c*, *d*, *e*, *g*, *x*, *y*, and *z* are parameters of the ignition and growth model. Both the reactive and unreactive components of the explosive use the JWL equation of state. The first term on the right-hand side of Equation (1) is the ignition term, describing the hot spot combustion stage; the second term is the growth term, describing the transfer of combustion from the hot spot to the internal and external particles; the third term is the bulk reaction term, describing the rapid transition from combustion to detonation. The material parameters of PBX9502 are provided in Table 1.

Table 1 PBX9502 material parameter (Tarver et al.2018)

I	*a*	*b*	*x*	G_1	*y*
4E6	0.214	0.667	7	0.6	1
c	*d*	G_2	*e*	*g*	*z*
0.667	0.111	400	0.333	1	3
Unreacted JWL	*A*/GPa	*B*/GPa	R_1	R_2	ω
	632.07	-0.04472	11.3	1.13	0.8938
Product JWL	*A*/GPa	*B*/GPa	R_1	R_2	ω
	13.6177	0.7199	6.2	2.2	0.5

The equation of state for JH-2 was modeled using the Jones-Wilkins-Lee (JWL) model:

$$p = A(1 - \frac{\omega}{R_1 V})e^{-R_1 V} + B(1 - \frac{\omega}{R_2 V})e^{-R_2 V} + \frac{\omega E}{V} \quad (2)$$

In the equation, *A*, *B*, R_1, R_2, ω are material parameters; *p* represents the pressure of the detonation products, *E* denotes the specific internal energy per unit volume, and *V* is the relative volume. The parameters for explosive JH-2 are provided in Table 2.

Table 2 JH-2 material parameter (Zhang et al.2025)

ρ/g·cm^{-3}	*D*/m·s^{-1}	*E*/J·mm^{-3}	P_{CJ}/GPa	*A*/GPa	*B*/GPa	ω	R_1	R_2
1.69	8425	8.5	29.5	852.4	18.2	0.38	4.6	1.3

The liner and 45# steel both adopt the Johnson-Cook (JC) strength model and the shock equation of state, which effectively describes the material behavior under conditions of large strain, high strain rate, and elevated temperature. The Johnson-Cook (JC) model is shown in Equation (3).

$$\sigma = (A + B\varepsilon^n)(1 + C\ln\frac{\dot{\varepsilon}}{\dot{\varepsilon}_0})(1 - T^{*m}) \quad (3)$$

Where *A* is the initial yield strength; *B* is the hardening modulus; *n* is the stress hardening exponent; *C* is the strain rate hardening coefficient; *m* is the thermal softening coefficient. The material parameters for the liner and 45# steel are presented in Table 3.

Table 3 45# steel and CU-OFHC material parameters (Jia et al.2019)

	ρ/g·cm^{-3}	G/GPa	A/GPa	B/GPa	n	C	m	$\dot{\varepsilon}_0$	γ	$C1$/ m·s^{-1}	$S1$
45#steel	7.83	7.7	0.352	0.3	0.014	0.26	1.03	1	2.17	4569	1.49
CU-OFHC	8.96	4.6	0.09	0.292	0.025	0.31	1.09	1	2.02	3940	1.489

The material parameters for air and RHA were obtained from the Autodyn material library, with those of RHA and air presented in Table 4 and Table 5, respectively.

Table 4 RHA material parameter

ρ/g·cm^{-3}	Γ	$C1$	$S1$	σ_s /GPa	G/GPa
7.86	1.67	4.61	1.73	1.5	64.1

Table 5 air material parameters

ρ/g·cm^{-3}	γ	E/KJ·m^{-3}
1.225×10^{-3}	1.4	206.8

2.2 EFP Forming Simulation

The simulation was conducted in two stages to simplify the process. First, a preliminary simulation of EFP formation was performed. The EFP formation simulation model is shown in Figure 1. The charge diameter is 150mm, the charge height is 125mm, the shell thickness is 5mm, and the liner is a dual-curve liner with a wall thickness of 4mm. A grid size of 0.6mm×0.6mm was used, and the unit system used was cm-g-μs. A flow-out boundary condition was applied to the air domain boundaries.

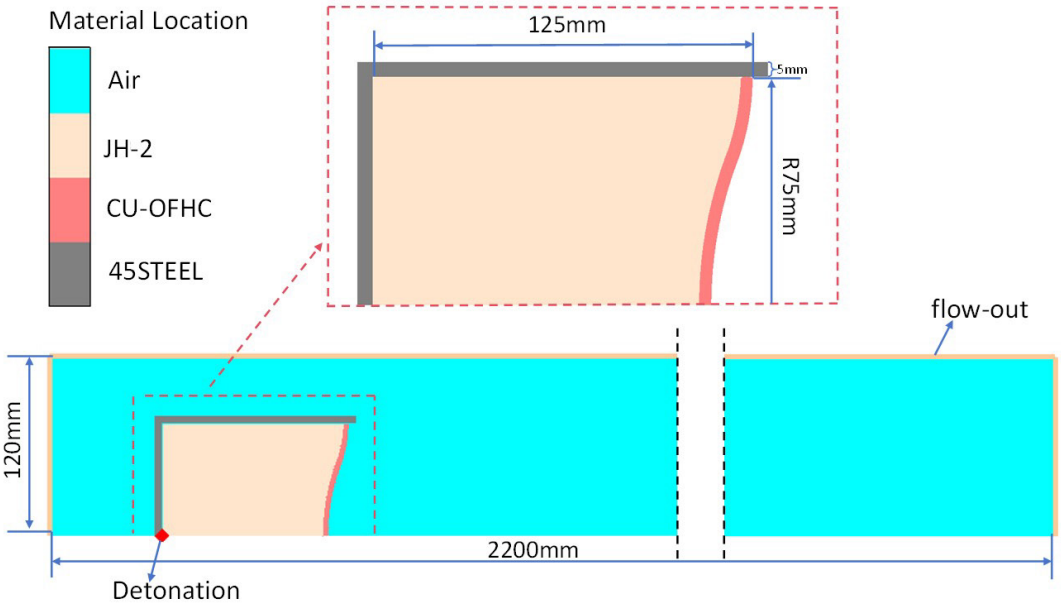

Figure 1 Simulation model

The numerical simulation of EFP formation is shown in Figure 2. From the figure, it can be observed that the liner flips and continues to stretch after the shaped charge detonation. At 602μs, the overall shape of the EFP was essentially established. At 693μs, the EFP reaches a stand-off distance of 1993.6mm, with an EFP velocity of 2850m/s. At this moment, the measured length of the EFP is 136.2mm, the diameter at the head is 24mm, and the maximum diameter at the tail is 58.8mm.

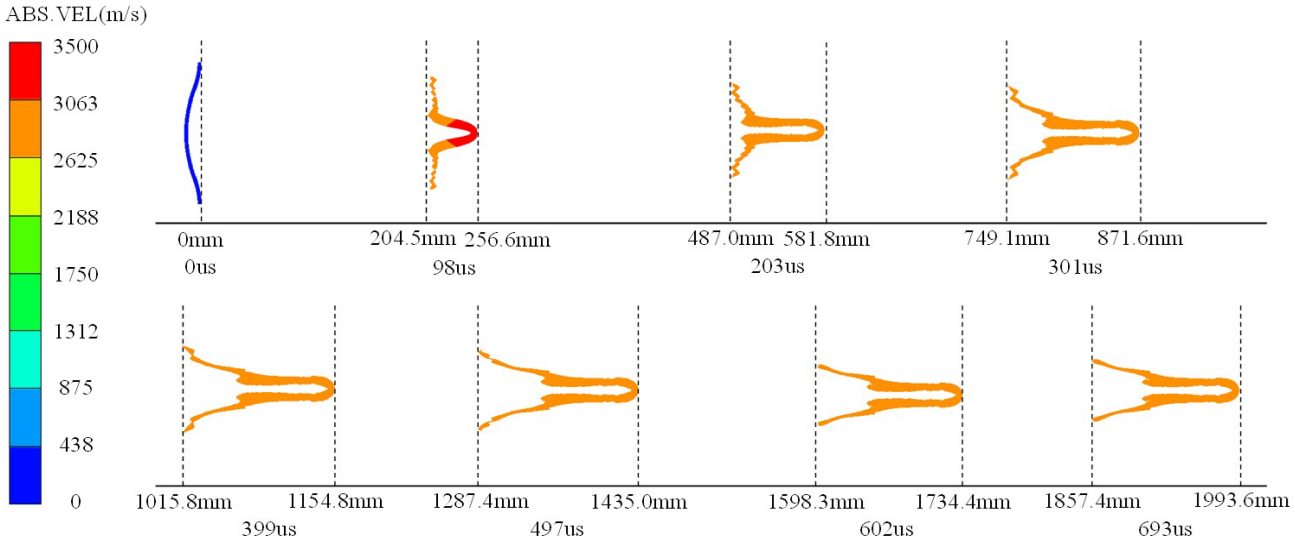

Figure 2 EFP formation

2.3 Study on the initiation of unconfined explosive by EFP

In numerical simulations, the simulation results for EFP generated by a specific shaped charge structure are identical, meaning that the velocity, shape, and other properties of the EFP are the same. Therefore, by adjusting the thickness of the cover plate and analyzing the pressure contour of the explosive, one can determine the degree of explosive reaction. When a detonation wave appears within the explosive and the pressure exceeds the CJ pressure of the explosive, it indicates that the explosive has undergone detonation. In this study, the CJ pressure of the PBX9502 is 27.47GPa (Tarver et al.2018).

A cover plate and acceptor charge were added after EFP formation to determine the critical thickness required for an EFP to initiate an unconfined explosive. The simulation model is shown in Figure 3. The acceptor charge has a diameter of 180mm and a thickness of 100mm. A series of gauges were placed within the acceptor charge to observe changes in pressure. The cover plate has a diameter of 300mm, and its thickness is represented by *H*. All times referenced in the subsequent text pertain to the moment following the EFP's contact with the cover plate.

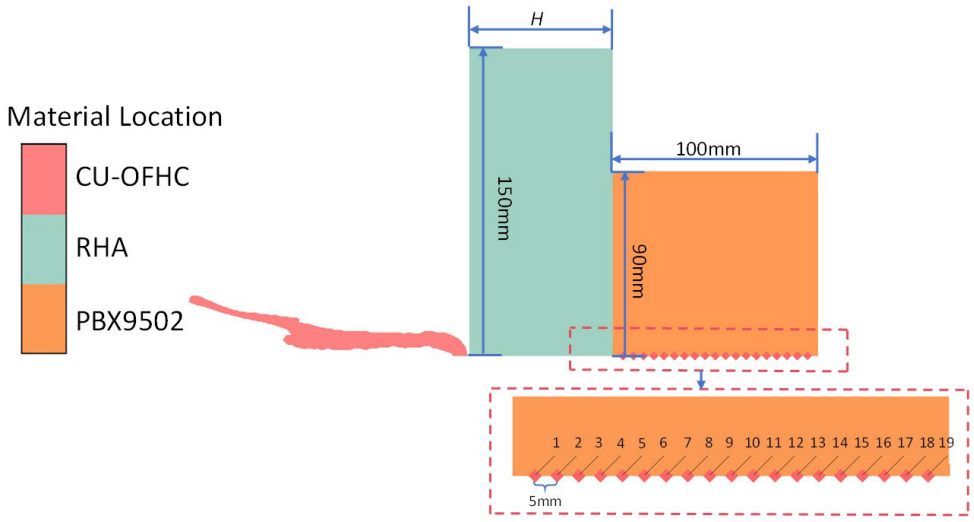

Figure 3 Numerical simulation model for the initiation of unconfined explosives by EFP

Pressure contour plots at different times for cover plate thicknesses of 10mm and 20mm are shown in Figure 4. When the cover plate thickness is 10mm, the explosive initiates at 4μs, but the EFP has not yet penetrated the cover plate. When the cover plate thickness is 20mm, the explosive initiates at 18μs, and again, the EFP has not penetrated the cover plate; however, a significant bulge forms on the backside of the cover plate.

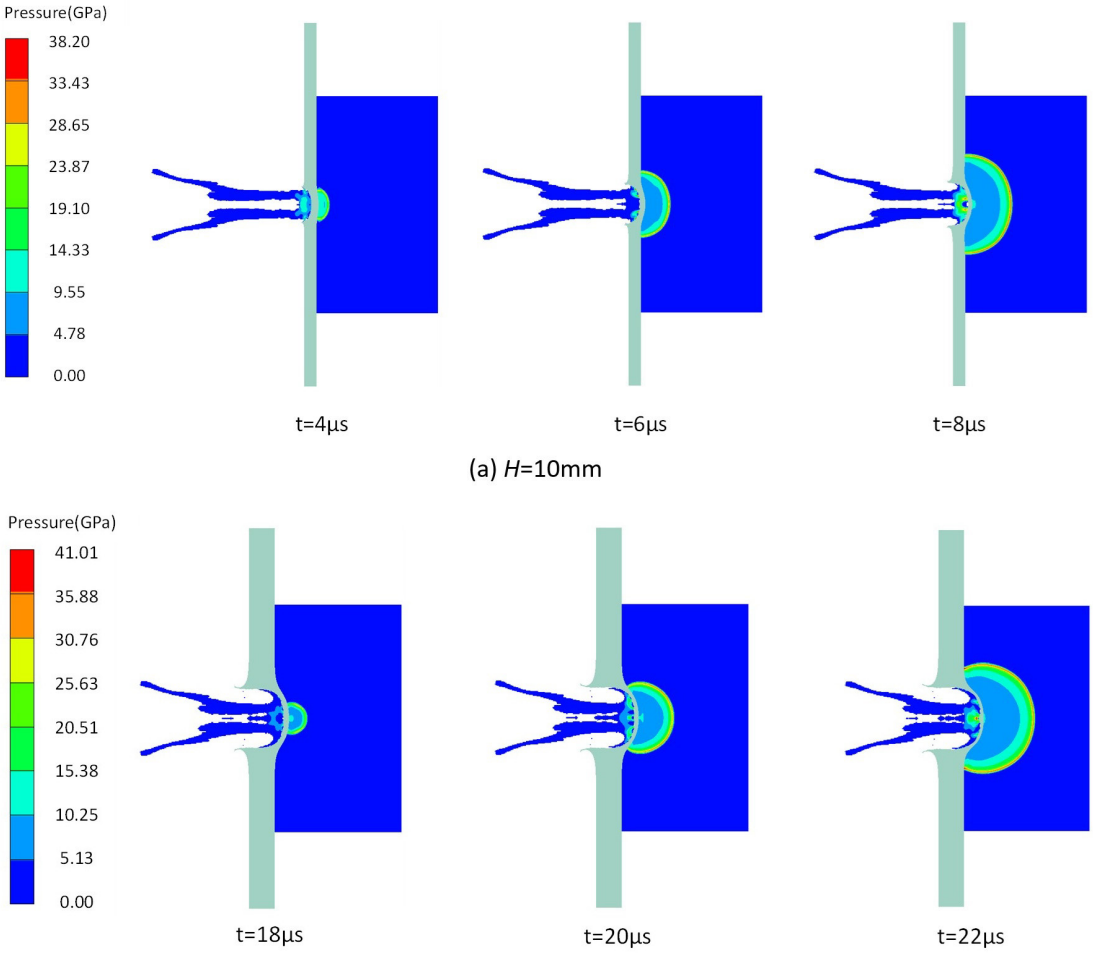

Figure 4 Pressure contour plots at various times for cover plates of 10mm and 20mm thickness

Pressure contour plots at different times for cover plate thicknesses of 30mm are shown in Figure 5. EFP initiates the explosive at 38μs, by which time the EFP has penetrated the cover plate and directly impacts the explosive. During the penetration process, the head of the EFP undergoes erosion, and the middle section takes on an annulus shape. When it interacts with the explosive, it generates an annulus detonation wave, which converges at the axis and further propagates within the explosive.

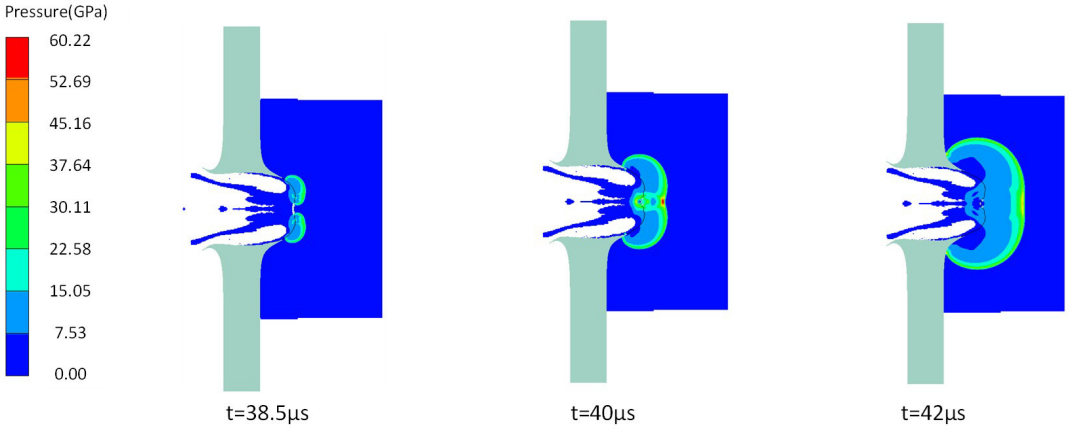

Figure 5 Pressure contour plots at various times for cover plates of 30mm thickness

The pressure curves at Gauge points for cover plate thicknesses of 30mm are shown in Figure 6. Since the initiation points are located on both sides of the axis, when the detonation waves reach the axis, they superimpose on each other, resulting in a detonation pressure significantly higher than the CJ pressure of the explosive. As the detonation waves propagate, the detonation pressure gradually decreases.

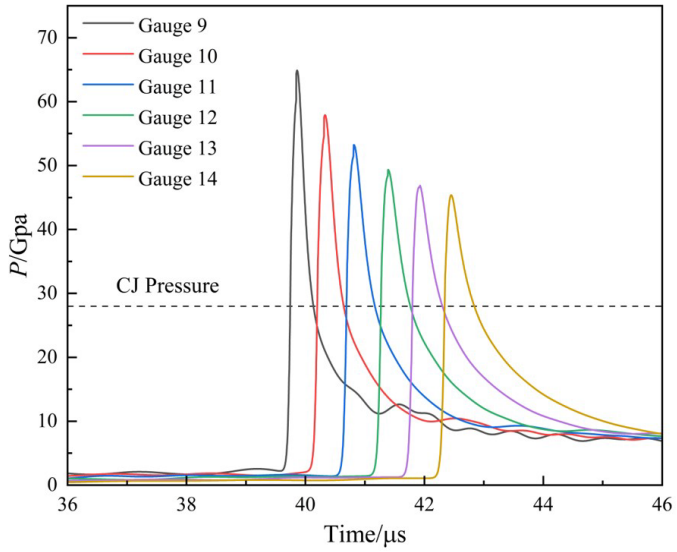

Figure 6 Pressure-time curve on the Gauge points

The initiation conditions of the explosive when the cover plate thicknesses are 40mm, 50mm, 60mm, and 70mm are illustrated in Figure 7. The initiation conditions are similar to those when the cover plate thickness is 30mm, where the EFP penetrates the cover plate and the remaining part of the EFP initiates the detonation of the explosive. The initiation points are located on both sides of the axis. It can also be observed that different cover plate thicknesses erode different lengths of the EFP, and EFP with varying cross-sections interact with the explosive.

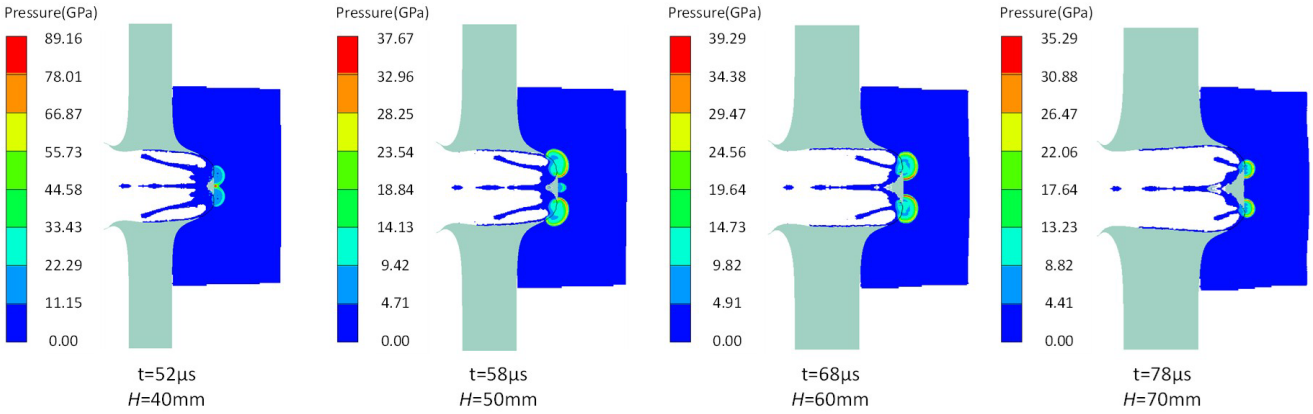

Figure 7 Pressure contour plots under cover plates of different thicknesses

The pressure contour plots at different time points for cover plate thicknesses of 84mm and 85mm are shown in Figure 8. After penetrating the cover plate, the EFP directly impacts the explosive, generating shock waves on either side of the explosive's axis. The pressure associated with these shock waves is lower than the CJ pressure of the explosive and thus the shock wave fails to initiate detonation. Subsequently, the shock waves converge along the axis, resulting in a gradual increase in pressure. When the cover plate thickness is 84mm, the pressure along the axis increases over time and exceeds the CJ pressure, leading to the formation of a detonation wave. In contrast, when the cover plate thickness is 85mm, the pressure along the axis decreases gradually and remains below the CJ pressure, failing to initiate the explosive.

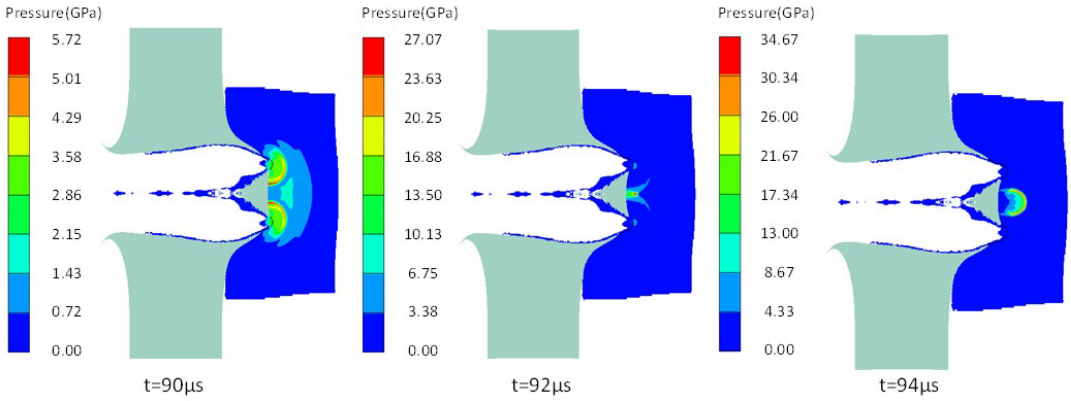

(a) *H*=84mm

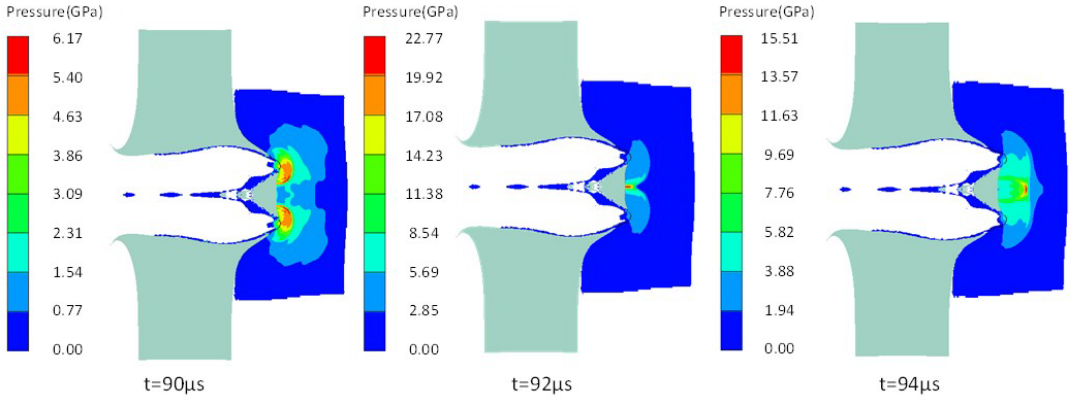

(b) *H*=85mm

Figure 8 Pressure contour plots at various times for cover plates of 84mm and 85mm thickness

The pressure curves at Gauge points for cover plate thicknesses of 84mm and 85mm are shown in Figure 9. The converging shock waves at the axis lead to an increase in pressure along the axis. When the cover plate thickness is 84mm, the maximum pressure at the axis of the explosive gradually increases and exceeds the CJ pressure of the explosive, indicating that the explosive is detonated. When the cover plate thickness is 85mm, the maximum pressure at the axis of the explosive gradually decreases, and the pressure falls below the explosive's CJ pressure, indicating that the explosive is not detonated. Therefore, the critical initiating cover plate thickness for unconfined explosives is determined to be 84mm.

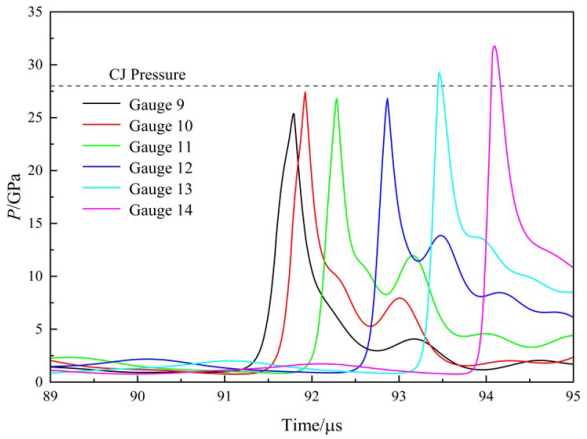

(a) *H*=84mm

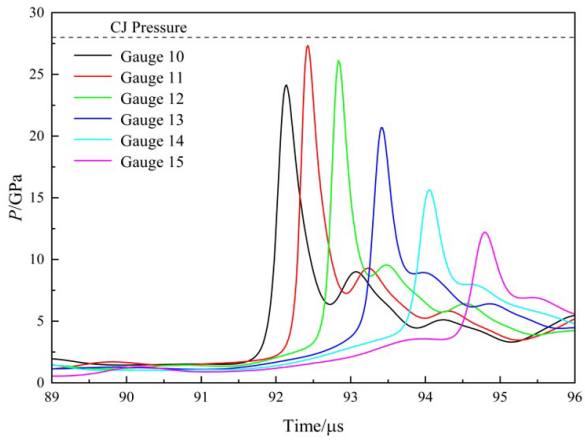

(b) *H*=85mm

Figure 9 Pressure-time curve on the Gauge points

2.4 Study on the initiation of confined explosive by EFP

In the simulation, a shell containing the acceptor charge was established to determine the critical initiation thickness of the cover plate for a confined explosive subjected to an EFP. The simulation model is shown in Figure 10, where the shell thickness is 10mm and the thickness of the post-effect target is 100mm.

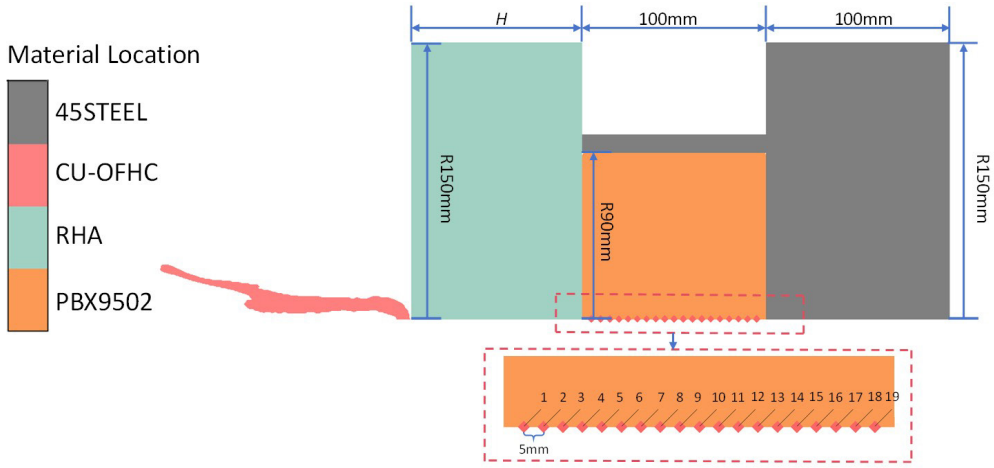

Figure 10 Numerical simulation model for EFP impact initiation of confined explosives

The pressure contour plots of explosive with a cover plate thickness of 90mm are shown in Figure 11. At 98μs, the maximum pressure in the explosive reaches 32.25GPa. At 101μs, the detonation wave develops at the bottom of the explosive, with a maximum pressure of 33.75GPa. Subsequently, the detonation wave reflects at the bottom of the explosive and propagates radially along the bottom surface of the explosive.

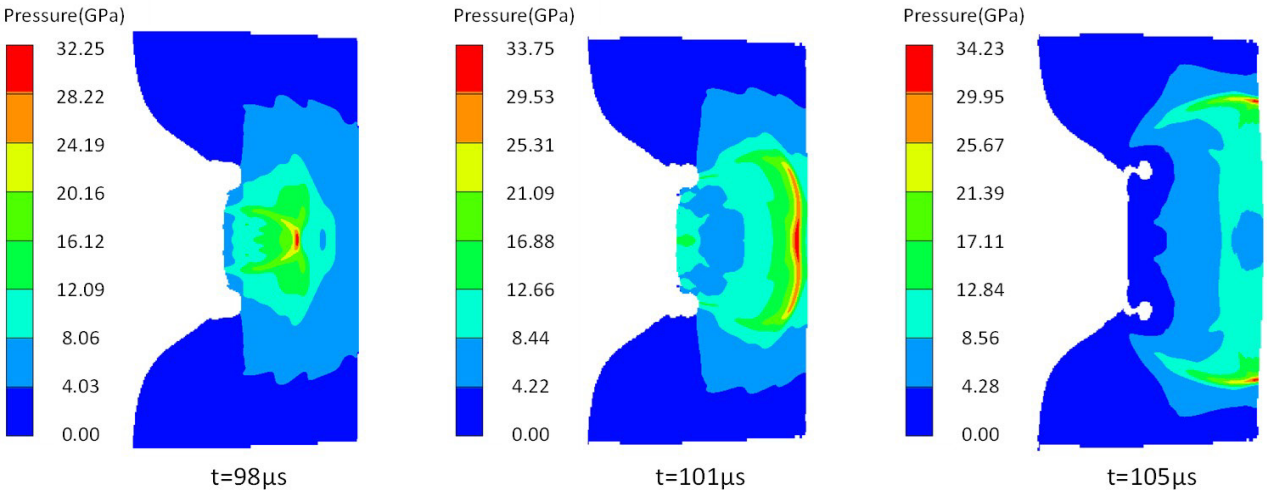

Figure 11 Pressure contour plots at various times for cover plates of 90mm thickness

The pressure contour plots of the explosive with cover plate thicknesses of 93mm and 94mm are shown in Figure 12. When the cover plate thickness is 93mm, the maximum pressure in the explosive reaches 28.12GPa at 100μs and then develops into a shock wave at 104μs with a pressure of 27.24GPa. After reflecting at the bottom of the explosive, a detonation wave forms and propagates along the bottom surface of the explosive. When the cover plate thickness is 94mm, the reaction of the explosive is similar to that with a 93mm cover plate thickness, but the maximum pressure after reflecting at the bottom of the explosive is only 25.17GPa. As this value is below the CJ pressure of the explosive, the shock wave fails to reach the threshold required for a self-sustained detonation and does not transition into a detonation wave. Therefore, it can be concluded that the critical initiation cover plate thickness for the impact initiation of confined explosive by an EFP is 93mm.

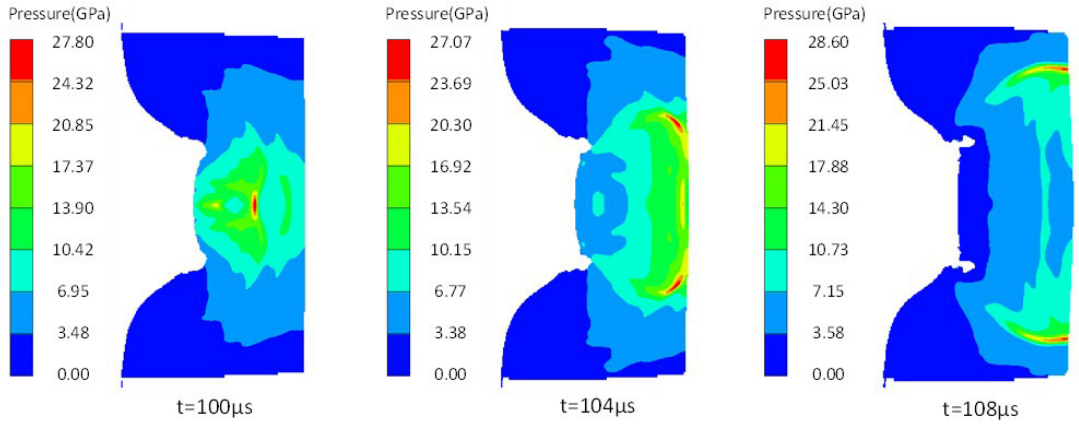

(a) *H*=93mm

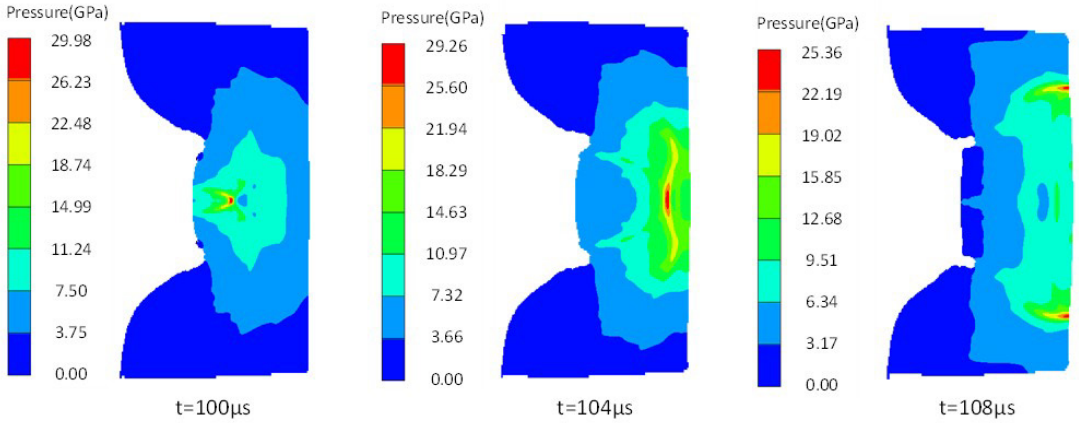

(b) *H*=94mm

Figure 12 Pressure contour plots at various times for cover plates of 93mm and 94mm thickness

The pressure contour plots of the explosive with a cover plate thickness of 100mm are shown in Figure 13. At 98μs, the maximum pressure in the explosive is 13.41GPa. At 104μs, after reflection by the shell, the maximum pressure in the explosive increases to 21.04GPa. Subsequently, the shock wave propagates along the bottom of the shell toward both sides, with a maximum pressure of 24.22GPa—which is lower than the CJ pressure of the explosive. Thus, the explosive did not undergo detonation; however, the formation of high-pressure shock waves confirms an explosion reaction occurred at this stage.

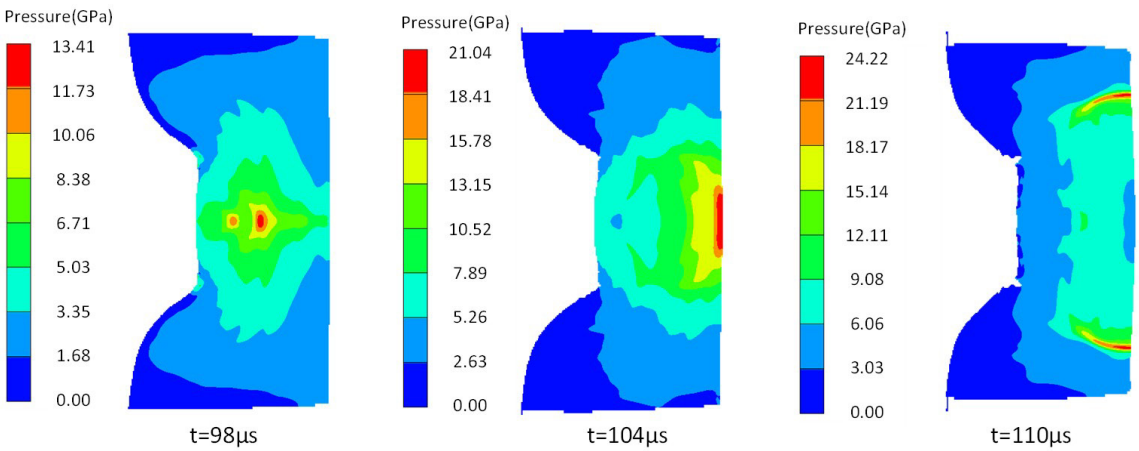

Figure 13 Pressure contour plots at various times for cover plates of 100mm thickness

The pressure contour plots of the explosive with a cover plate thickness of 110mm are shown in Figure 14. The pressure-time curve at the Gauge points within the explosive is shown in Figure 15. It can be observed that the maximum pressure within the explosive is only 7GPa, and no detonation wave is detected within the explosive. This indicates that the charge did not undergo detonation or explosion.

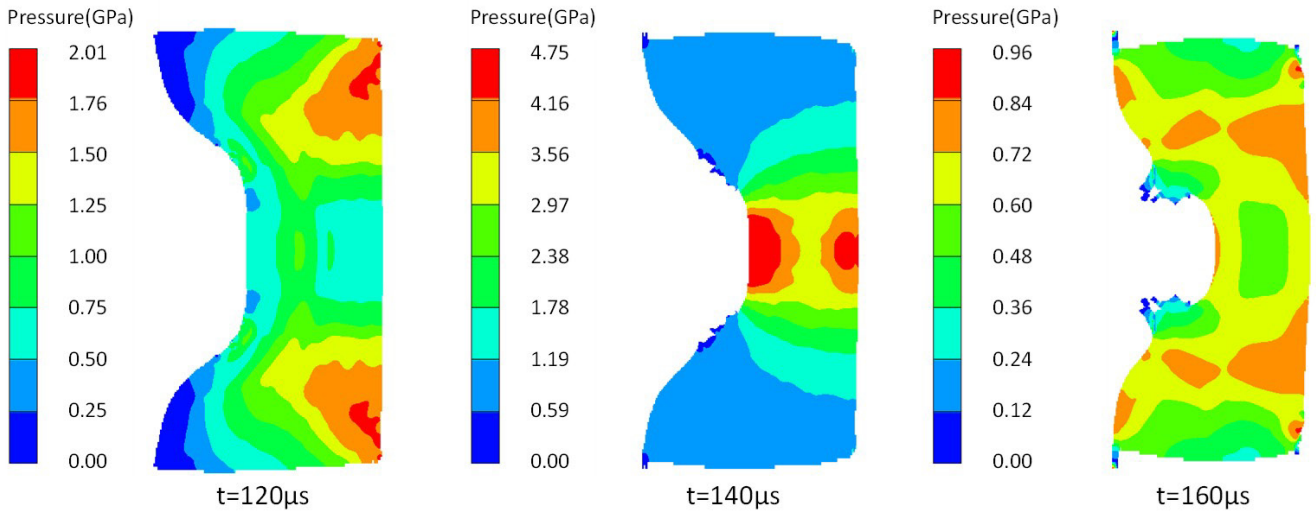

Figure 14 Pressure contour maps at various times for cover plates of 110mm thickness

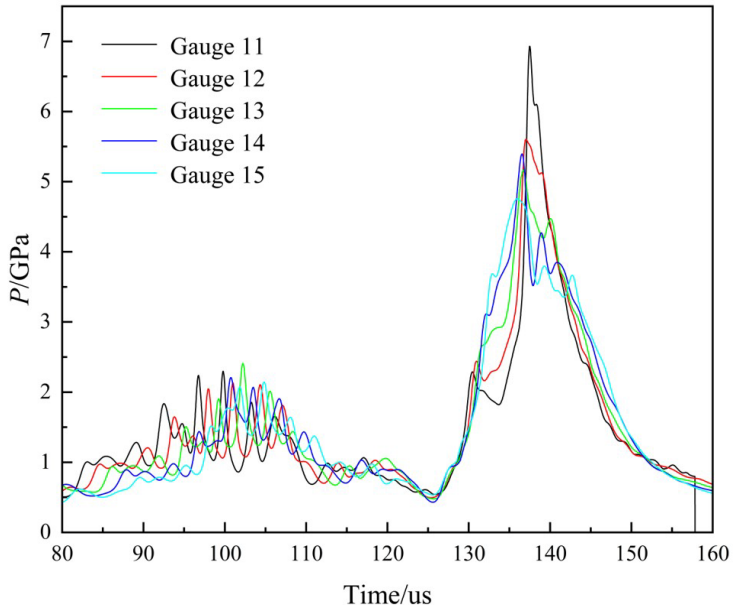

Figure 15 Pressure-time curve on the Gauge points

2.5 Analysis of simulation results

For unconfined explosives, when the cover plate is relatively thin, the head of the EFP impacts the cover plate, generating a shock wave that propagates into the explosive and initiates it. When the cover plate thickness is 10mm and 20mm, the EFP initiates the explosive without penetrating the cover plate.

When the cover plate is thicker, the shock wave rapidly attenuates, making it difficult to initiate the explosives. The EFP must penetrate the cover plate, and the residual portion directly impacts the explosive to cause detonation. A key aspect of this process is that different cover plate thicknesses erode different lengths of the EFP, causing distinct cross-sections along the EFP to interact with the explosive. The extent of this erosion is influenced by the material behavior described by the Johnson-Cook model: strain-rate hardening helps the EFP maintain its integrity to penetrate thicker

plates, while thermal softening promotes the head's erosion. For the EFP in this study, which has an annular middle and tail section, thicker cover plates erode the solid head of the EFP, ultimately allowing the annular cross-section to impact the explosive and create a characteristic annulus detonation wave.

For confined explosives, due to the presence of the shell, the waves formed in the explosive are reflected at the shell, increasing the pressure in the explosive and making it easier to develop into detonation. Additionally, compared to unconfined explosives, the shell prevents the transmission of rarefaction waves from the bottom of the explosive, avoiding the unloading of pressure in the explosive by these waves. In summary, the critical initiation threshold for confined explosives is lower, and the corresponding critical initiation cover plate thickness is larger.

3 ENGINEERING MODEL FOR THE CRITICAL THRESHOLD OF EXPLOSIVE INITIATION BY EFP

For different cover plate thicknesses, different cross-sections of the EFP will directly impact the explosive. The velocity and diameter of the EFP's cross-section as it impacts with the explosive vary, resulting in different v^2d values for different cross-sections and different abilities to initiate the explosive. By considering the cross-sections with v^2d values greater than the critical initiation threshold of the explosive as effective cross-sections, we can obtain the effective length of the EFP. The penetration depth corresponding to its effective length represents the critical cover thickness for initiating explosives by an EFP. Therefore, the velocity v and diameter d of different EFP cross-sections directly acting on the explosive are key to solving this problem.

3.1 Equivalent diameter of different cross-sections of an EFP

In this paper, the EFP studied has a circular cross-section at its head, while the middle and tail sections are annular in shape. Therefore, this type of EFP will be the focus of our research. In the v^2d criterion, d represents the diameter of a solid cylinder. Hence, it is necessary to equate the inner and outer diameters of the annulus to an equivalent diameter of a solid cylinder. There is limited research on the interaction of annular cross-sections with explosives. Held (M. Held,1984) proposed that the critical initiation velocity is inversely proportional to the fourth root of the acting area, but this relationship does not hold for annular shapes. However, it is believed that the equivalent diameter of an annulus is related to the diameter of a cylinder with the same area. This relationship can be expressed as:

$$d = \sqrt{{d_2}^2 - {d_1}^2} f(d_1, d_2) \tag{4}$$

Where d is the equivalent diameter, and d_1 and d_2 are the inner and outer diameters of the annulus, respectively.

Throughout the simulations, the area of the annulus was held constant to establish the relationship between its inner/outer diameters and the equivalent diameter. Eight different outer diameter values (d_2 = 20~80mm) were selected, and the corresponding inner diameter d_1 was derived using the annular area formula. Subsequently, simulations were conducted on the shock initiation of explosives by annuluses with varying inner and outer diameters. A series of equivalent diameters corresponding to different inner and outer diameter combinations were obtained, and the relationship between the inner and outer diameters of the annulus and its equivalent diameter was finally obtained through fitting using Origin software. The equivalent diameters corresponding to annuluses with different inner and outer diameters are shown in Table 6, and the fitted curve is illustrated in Figure 16.

Table 6 Equivalent diameters correspond to annuluses with different inner and outer diameters

Inner diameters d_1/mm	Outer diameters d_2/mm	Equivalent diameters d/mm
0	20	20
9.165	22	16.66
16.614	26	14.15
22.36	30	12.33
29.94	36	10.54
34.64	40	9.25
56.56	60	6.23
77.46	80	5.22

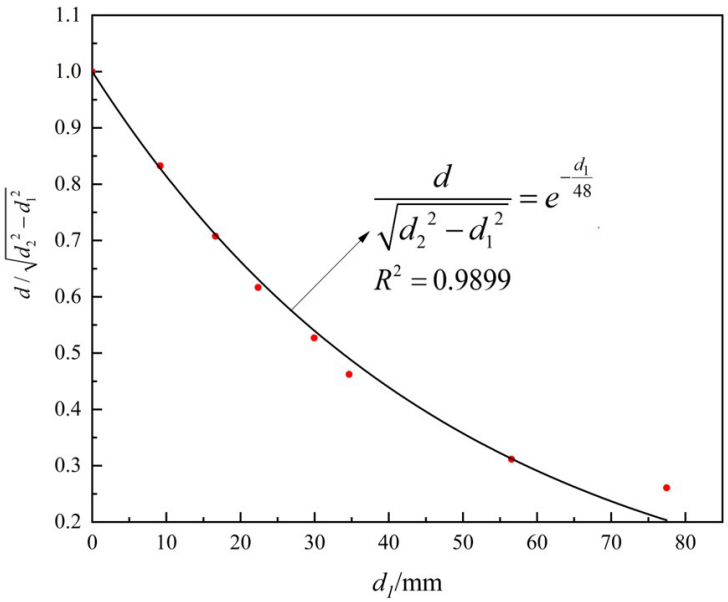

Figure 16 Plot of fitted curve

The fitted relationship between the inner and outer diameters of the annulus and its equivalent diameter is:

$$d=\sqrt{d_2^{\,2}-d_1^{\,2}}\times e^{-\frac{d_1}{48}} \tag{5}$$

Based on the simulation results, the structure of the EFP can be obtained. Due to the complexity of the middle section of the EFP, certain simplifications were made. The structure of the EFP and its inner and outer surface are shown in Figure 17.

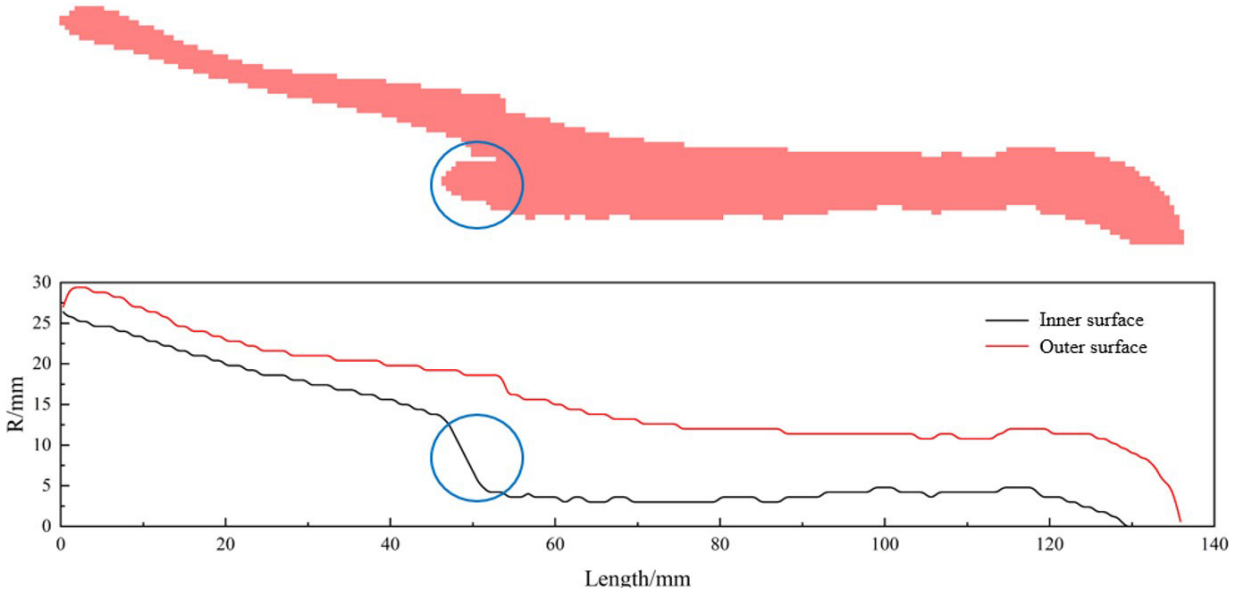

Figure 17 The structure of the EFP and its inner and outer surface

By substituting the inner and outer diameters of different cross-sections of the EFP into equation (5), the equivalent diameters of those cross-sections can be obtained. The inner diameter, outer diameter, and equivalent diameter corresponding to different axial positions of the EFP are shown in Figure 18.

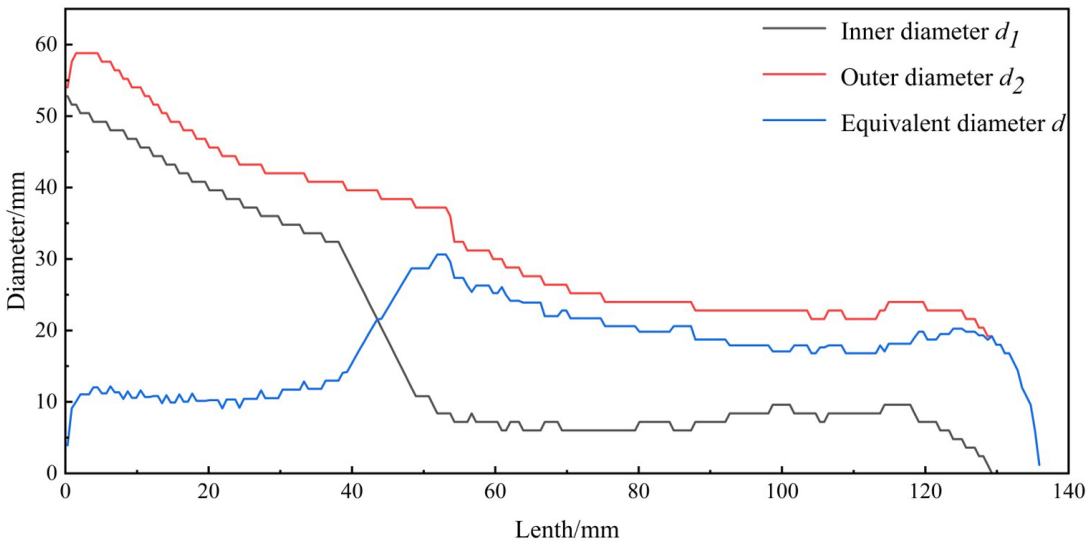

Figure 18 The inner diameter, outer diameter, and equivalent diameter of the EFP

3.2 The velocities at different cross-sections of the EFP

The penetration process of an EFP into an RHA plate is highly complex. To simplify the calculation process, the A-T penetration model is used to calculate the penetration of an EFP into an RHA cover plate. The A-T model is primarily applicable to the penetration of long-rod projectiles into target plates. However, in this study, the EFP exhibited dynamic erosion characteristics similar to those of long-rod projectiles during the penetration of the cover plate. Specifically, during high-speed penetration, the material at the head of the EFP undergoes continuous erosion due to plastic flow and thermal softening effects, and its axial stress distribution is comparable to the hydrodynamic behavior of long-rod projectiles. Li et al. (2018) employed the A-T penetration model to calculate the penetration of EFP into target plates and reported good agreement with experimental data. Therefore, the A-T penetration model is used to calculate the penetration of EFP.

TATE (1967) and ALEKSEEVSKII (1966) introduced projectile and target strength parameters into the one-dimensional fluid Bernoulli equation, establishing the axial stress balance relationship at the projectile-target interface during the ultra-high-speed penetration of a long rod projectile into a metal target. This is known as the one-and-a-half-dimensional fluid dynamics A-T model:

$$\frac{1}{2}\rho_p(v-u)^2 + Y_p = \frac{1}{2}\rho_t u^2 + R_t \tag{6}$$

In the equation, ρ_p and ρ_t represent the densities of the projectile and target materials, respectively. v and u represent the instantaneous rigid penetration velocity at the tail of the projectile and the instantaneous penetration velocity at the head of the projectile (the projectile-target contact interface), respectively.

The A-T model assumes that during high-speed penetration, the contact interface area between the projectile and the target behaves like a fluid, and the projectile undergoes erosion. The governing equation is:

$$\frac{dv}{dt} = -\frac{Y_p}{\rho_p l} \tag{7}$$

$$\frac{dP}{dt} = u \tag{8}$$

$$\frac{dl}{dt} = -(v-u) \tag{9}$$

In the equation, P and l represent the instantaneous penetration depth and length of the projectile, respectively.

During the penetration process, the EFP undergoes continuous erosion, resulting in a gradual decrease in its velocity. For different thicknesses of the RHA plate, the remaining length and velocity of the EFP will vary. Using the A-T penetration model, the velocity corresponding to different remaining lengths of the EFP can be calculated. Relevant parameters are shown in Table 7, and the calculation results are illustrated in Figure 19.

Table 7 Parameters of projectiles and targets

	ρ/g·cm^{-3}	Parameters of the A-T model
EFP	8.96	Y_p = 0.8GP (Zhang,2005)
RHA	7.85	R_t = 5.3GPa (Zhai,2017)

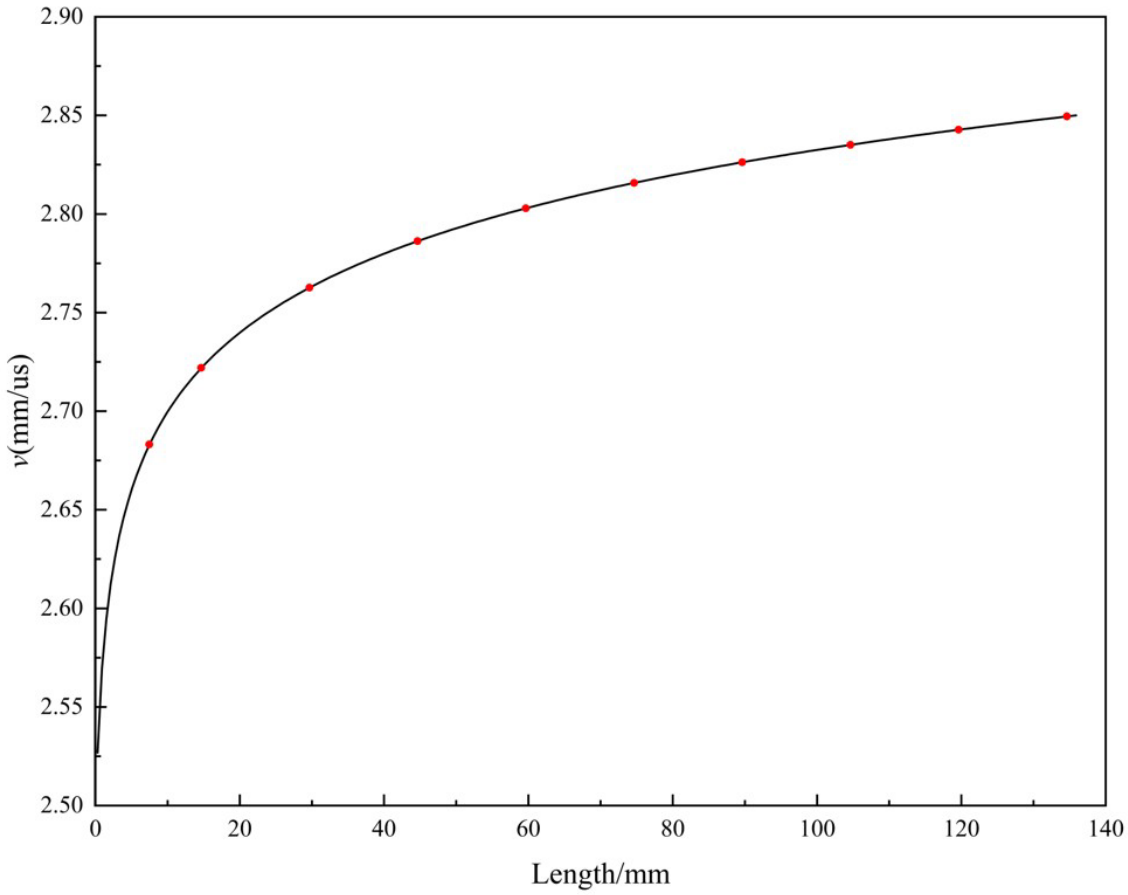

Figure 19 The velocity corresponding to different remaining lengths of the EFP

The velocity corresponding to different remaining lengths of the EFP refers to the velocity at which different cross-sections of the EFP interact with the explosive. Since there is no analytical solution for the A-T penetration model, the velocity at different cross-sections is represented as $v(l)$.

3.3 Critical initiation threshold model

By multiplying the square of the velocity $v(l)$ at different cross-sections by the equivalent diameter d of those cross-sections, we can obtain the v^2d values for different cross-sections. The v^2d values for different cross-sections are shown in Figure 20. Previous research has shown that the initiation threshold for confined explosives is lower than that for unconfined explosives. Therefore, to characterize the influence of the casing on the initiation threshold of the explosive, a coefficient α is added. When the explosive is unconfined, α equals 1. The final expression is:

$$\alpha I_{cr} = v(l)^2 d \tag{10}$$

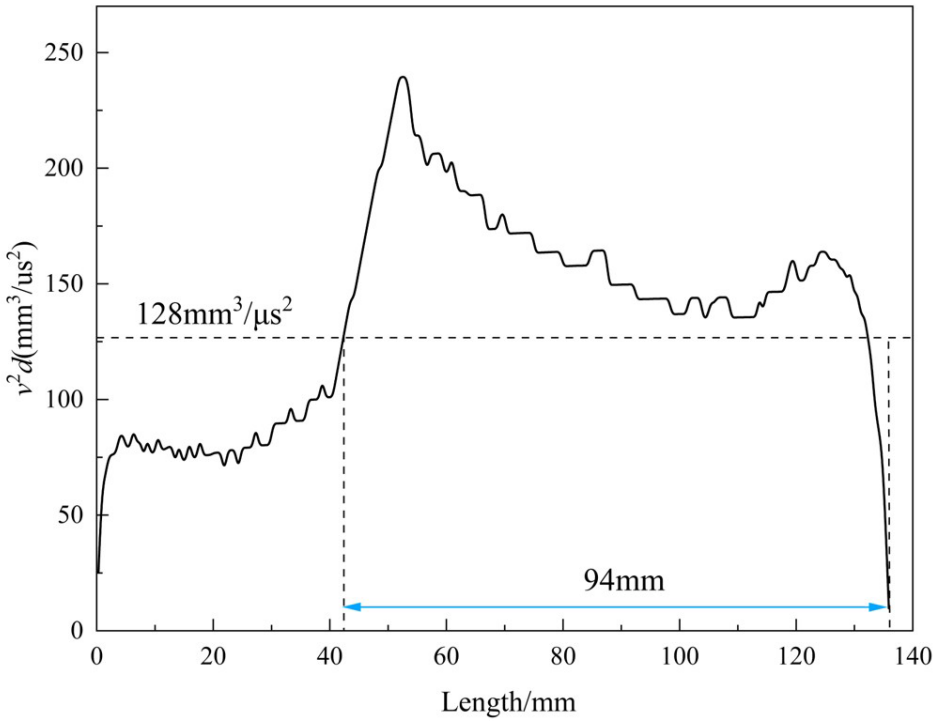

Figure 20 The v^2d values at different cross-sections

M. Held (1989) indicates that the critical initiation threshold for PBX9502 is 128mm^3/μs^2. For unconfined explosive, substituting this critical initiation threshold into equation (10) yields two mathematical solutions for the length of the EFP, as illustrated in Figure 20. The v^2d curve intersects the critical threshold at two distinct points, indicating the non-uniqueness of the solution. However, the intersection corresponding to the EFP head is invalid, since the head—with its near-spherical geometry—initially exhibits a v^2d value below the critical threshold and undergoes erosion during penetration, preventing it from directly impacting the explosive. Therefore, only the second intersection point is considered meaningful, resulting in an effective EFP length of 94mm for critical initiation. Based on the A-T penetration model, the corresponding penetration depth is calculated to be 75.56mm, which indicates that the critical cover thickness for initiating an unconfined explosive with an EFP is 75.56mm. The simulated critical cover thickness is 84mm, suggesting a certain discrepancy between the engineering model and the simulation results. In this paper, the A-T penetration model is applied to calculate the penetration of the EFP. However, this model was originally designed for solid long-rod projectiles penetrating semi-infinite targets, while the EFP studied herein features a hollow annular cross-section that is inherently inconsistent with the model's basic assumptions. The study by Kim et al. (2011) demonstrated that higher EFP solidity leads to greater penetration depth, a factor not incorporated in the traditional A-T model. Therefore, the model's failure to account for the EFP's unique hollow annular geometry and its inherently low solidity is a primary source of error. Future research will focus on the penetration mechanism of hollow EFP to establish a more accurate calculation model.

For confined explosives, the simulated critical initiation cover thickness is 93mm. Using the A-T penetration model in reverse, the corresponding length is deduced to 114.5mm, with a remaining EFP length of 21.7mm. The corresponding v^2d value for this remaining length is 77mm^3/μs^2, from which an α value of 0.602 can be derived.

4 EXPERIMENTS

4.1 Experimental setup

Experiments were conducted to validate both the simulation and engineering models. The tests involved EFP impact initiation of explosives with cover plates of varying thickness. The EFP shaped charge used in the experiments consisted of a liner, explosive, and shell, with a diameter of 160mm, a shaped charge diameter of 150mm, and a shell thickness of 5mm. The photograph of the shaped charge is shown in Figure 21. The explosive employed was JH-2, pressed into shape with a density of approximately 1.69g/cm^3. The liner material was oxygen-free high conductivity copper.

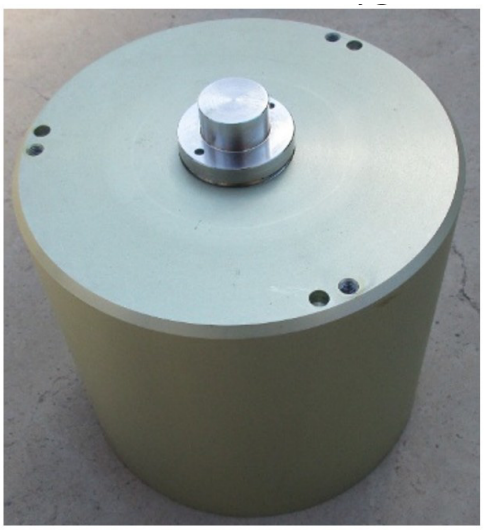

Figure 21 The photograph of the shaped charge

The structure of the explosive container is shown in Figure 22. For convenience of experimental setup, the explosive container is designed as a square-section shell with one open end, featuring a wall thickness of 10mm and overall dimensions of 300mm×300mm×110mm. A wooden plate with a central circular hole is installed inside the shell cavity. The acceptor charge, along with its shell, is embedded into the circular hole in the wooden plate. Specific parameters of the acceptor charge are as follows: a diameter of 180mm, a height of 100mm, and a shell thickness of 10mm. To achieve sealing protection, a layer of wax paper is placed over the open end of the explosive box and secured with adhesive tape.

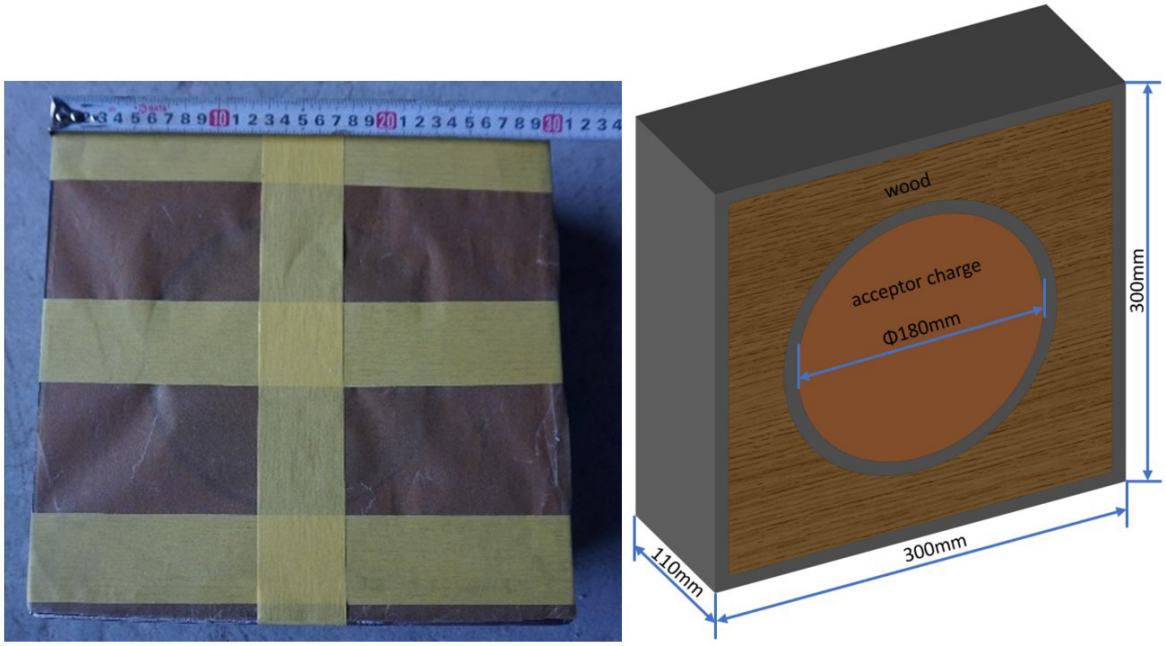

Figure 22 The structure of the explosive container

The experimental setup is shown in Figure 23. The standoff distance is 2 meters. Two velocity measurement targets are set up between the EFP shaped charge and the target to obtain the flight velocity of the EFP. The distance between the two velocity measurement targets is 500mm. A high-speed camera, model Phantom-VEO710, is placed 50meters away to record the initiation of the explosives. The camera operates at a frame rate of 1,000,000 frames per second. The ambient temperature at the test site is 15°C, and the atmospheric pressure is 101KPa. The target sequence from front to back consists of an RHA cover plate, an explosive container, and a 45# steel after-effect target.

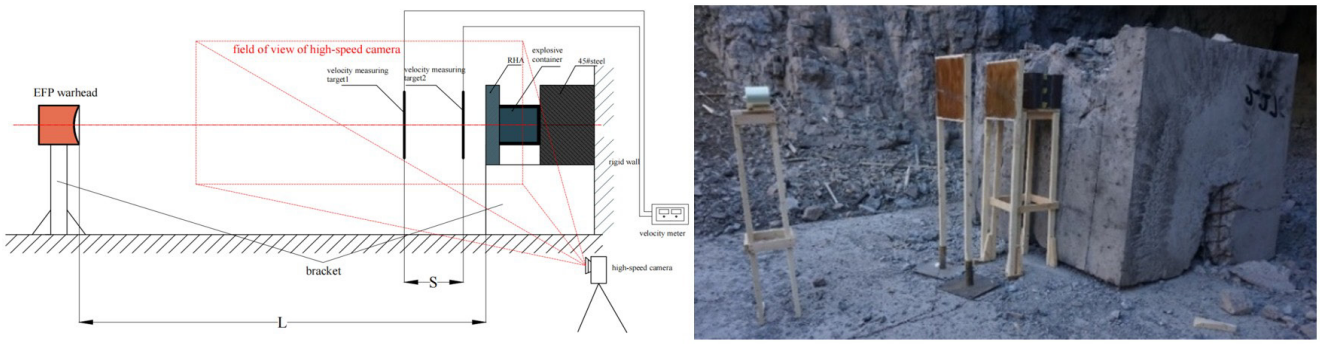

Figure 23 Diagram of experimental layout

A total of four tests were conducted with different cover plate thicknesses, namely 50mm, 90mm, 100mm, and 110mm. Among these, the 110mm cover plate was composed of one 90mm cover plate and two 10mm cover plates.

4.2 Experimental results and analysis

High-speed photography results obtained under different experimental conditions are presented in Figure 24, which captures sequential high-speed images of the EFP impacting the cover plate and the subsequent explosive reaction. The high-speed images reveal the following observations: When the cover plate thicknesses are 50mm, 90mm, and100mm, after the EFP impacted the cover plate, an intense fire flash emitted from the acceptor charge was observed, and the scope of the fire flash rapidly expanded, indicating a violent reaction of the acceptor charge. When the cover plate was 110mm, after the EFP impacted the cover plate, no intense fire flash was emitted, but a large amount of black smoke surrounded the area, indicating that the explosive did not undergo a violent reaction at this time.

The damage patterns of the after-effect targets and explosive containers under different experimental conditions are shown in Figure 25 and Figure 26. When the cover plate thickness was 50mm, a circular pit formed at the center of the after-effect target, and a large crater with some bending was observed in the middle of the bottom plate of the explosive container. At a cover plate thickness of 90mm, the after-effect target fractured and collapsed, accompanied by an indentation approximately 165mm in diameter. The corresponding explosive container was not recovered. When the cover plate thickness was 100mm, the after-effect target cracked but did not collapse, and the bottom plate of the explosive container showed penetration mark and indentation approximately 172mm in diameter. When the cover plate thickness was 110mm, there was no significant reaction observed on either the after-effect target or the bottom plate of the explosive container.

By combining the high-speed photography results and the damage patterns of the after-effect targets, the degree of explosive reaction under different experimental conditions can be obtained, as shown in Table 8 of test results. When the cover plate thickness is 50mm and 90mm, detonation occurred in the explosive; when the cover plate thickness is 110mm, deflagration occurred in the explosive; when the cover plate thickness is 100mm, the explosive underwent a violent reaction but based on the damage to the after-effect target and the bottom plate of the explosive container, the degree of reaction was lower than that when the cover plate thickness is 90mm. Therefore, it is considered that an explosion occurred in the explosives when the cover plate thickness is 100mm. It can be determined that the critical initiation cover plate thickness for the explosives is between 90mm and 100mm.

In the experiment, four velocity measurements were performed on the EFP, with the measured velocities being 2476m/s, 2678m/s, 2840m/s, and 2937m/s, respectively. The average velocity of the EFP was calculated as 2732.75m/s, with a standard deviation of 202m/s and a relative standard uncertainty of ±7.4%. Analysis suggests that this variability might be attributed to the processing errors in the shaped charges of different conditions, as well as the potential errors introduced by the use of velocity-measuring targets for EFP velocity measurement. In the simulation, the velocity of the EFP is 2850m/s, which deviates from the average experimental velocity of 2732.75m/s by only 4.3%. This minor discrepancy substantiates the accuracy of the simulation model. In the experiment, the explosive underwent detonation when the cover plate thickness was 90mm, and it exploded when the cover plate thickness was 100mm. In the simulation, detonation occurred in the explosive when the cover plate thickness was 90mm and 93mm, while explosion took place when the cover plate thickness was 94mm and 100mm. Moreover, in both the simulation and the experiment, the explosive underwent no reaction when the cover plate thickness was 110mm. The close agreement between the simulation and experimental results further verifies the correctness of the simulation model and the engineering model.

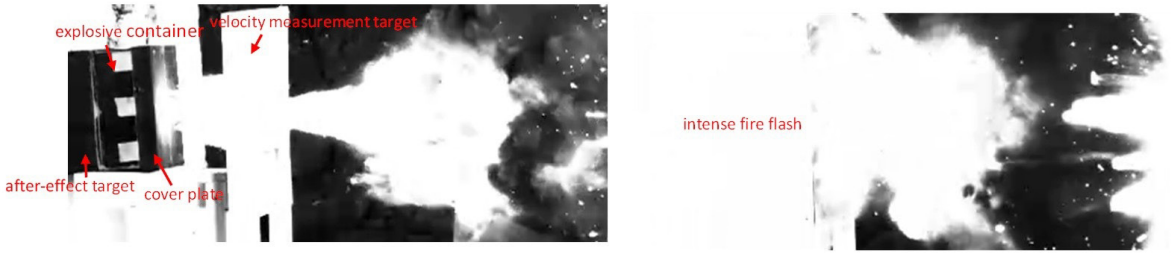

(a) *H*=50mm

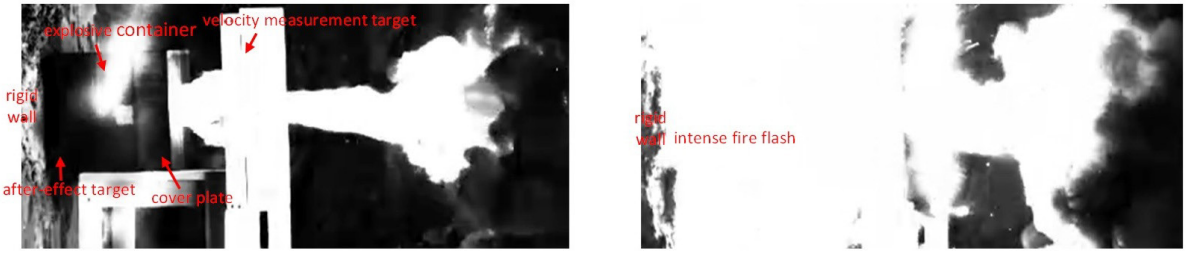

(b) *H*=90mm

(c) *H*=100mm

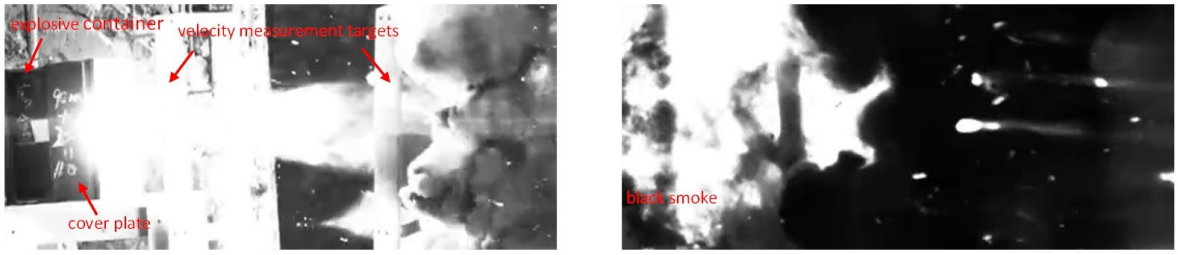

(d) *H*=110mm

Figure 24 High-speed photography results under different thicknesses of cover plate

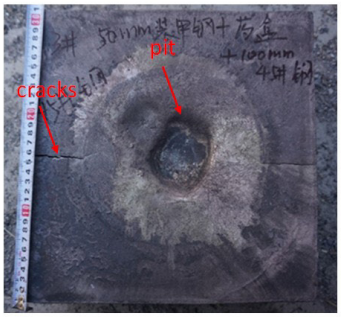

(a) *H*=50mm

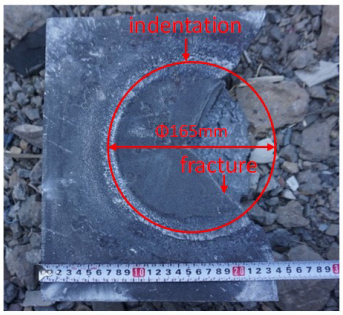

(b) *H*=90mm

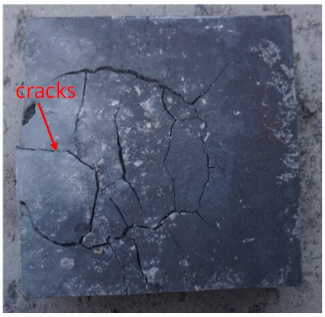

(c) *H*=100mm

Figure 25 Damage patterns of the after-effect targets

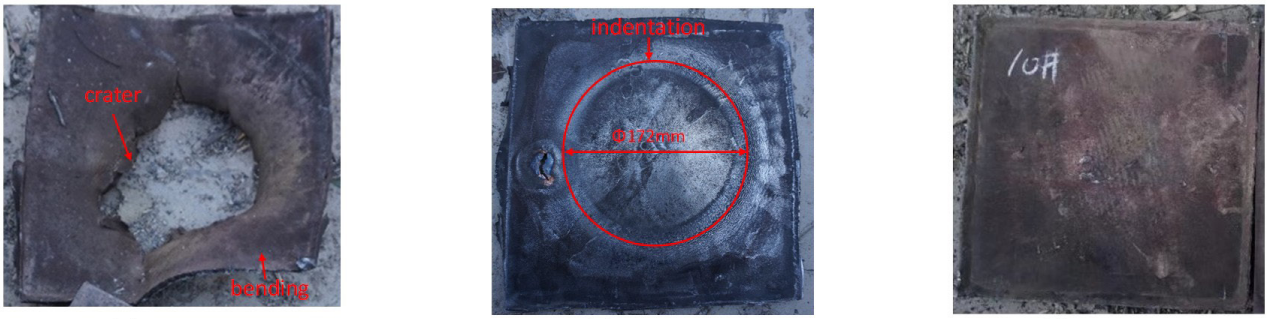

(a) *H*=50mm (b) *H*=100mm (c) *H*=110mm

Figure 26 Damage patterns of explosive containers

Table 8 Experimental results

The thickness of cover plate/mm	The velocity of EFP/m·s^{-1}	The average velocity of EFP/m·s^{-1}	Aftereffect target	Response level
50	2476	2732.75	Obvious dent	Detonation
90	2678		Fracture, Collapse, and Indentation	Detonation
100	2840		Crack	Explosion
110	2937		No reaction	No reaction

5 Conclusion

This study investigated the impact initiation of explosives by EFP, integrating experimental methods with numerical simulations conducted in Autodyn. The main conclusions are as follows:

(1) The initiation mechanisms of EFP on explosives with different cover plate thicknesses are different. As the cover plate thickness increases, the initiation mechanism transitions from explosive initiation by shock wave generated by EFP impact to explosive initiation by the remaining EFP after it penetrates the cover plate.

(2) A calculation method for the equivalent diameter of EFP with annular cross-section in impact initiation is proposed, realizing the mechanical equivalence between the annular cross-section and the solid cylinder through simulation data fitting to meet the application requirements of the Held criterion.

(3) Integrating the A-T penetration model and the Held criterion, an engineering model for the critical initiation threshold of EFP impact initiation of explosives is established, which can effectively predict the critical cover plate thickness.

ACKNOWLEDGEMENT

The study is funded by National Key Laboratory of Air-based Information Perception and Fusion (No. 202469)

Author's Contributions: Conceptualization, Guangyu Qian; Investigation, Guangyu Qian and Bin Ma; Writing-original draft, Guangyu Qian; Methodology, Guangyu Qian; Test technical support, Bin Ma; Writing-review & editing, Guangyu Qian and Bin Ma; Supervision, Bin Ma; Funding acquisition, Bin Ma.

Data availability statement: Research is only available upon request.

Editor: Rogério José Marczak

References

Walker, F. E., & Wasley, R. J. (1976). A general model for the shock initiation of explosives. Propellants, Explosives, Pyrotechnics, 1(4), 73-80.

James, H. R. (1996). An extension to the critical energy criterion used to predict shock initiation thresholds. Propellants, explosives, pyrotechnics, 21(1), 8-13.

Held, M. (1991). Diagnostics of the reaction behaviour of Less Sensitive High Explosives under jet attack. Propellants, explosives, pyrotechnics, 16(3), 131-139.

Held, M. (1996). Initiation criteria of high explosives at different projectile or jet densities. Propellants, Explosives, Pyrotechnics, 21(5), 235-237.

Chick, M. C., Bussel T, Frey R B, et al. (1986). Initiation of munitions by shaped charge jets. Proceedings of the 9th International Symposium on Ballistics. England, 421-430.

Chen, S. M., Jia, X., Xia, M., et al. (2021). Critical Initiation Threshold of Covered Finite Thickness Explosive under Impact of Shaped Charge Jet. Propellants, Explosives, Pyrotechnics, 46(10), 1572-1580.

Chen, S. M., Jia, X., Huang, Z. X., et al. (2022). Initiation of a Confined Finite Thickness Explosive under the Impact of Shaped Charge Jet. Propellants, Explosives, Pyrotechnics 47.4: e202100315.

Zhang, X. F., Zhao Y. S., Chen H. W. (2006). The Critical Condition of Shelled Explosive Initiated by Projectile, J. Journal of Balls,18(4): 57-59.

Chick, M. C., Bussell, T. J. (1988). The effect of minimum detonation diameter on the mechanism of jet initiation of bare explosives. J. Appl. Phys; 63 (9): 4761–4763.

Fang, Q., Wei, Y. Z., Zhang, K. (1997). An investigation on the projectile impact initiation mechanism of detonation in explosive charges covered with a thick steel plate. Journal of Ballistics 9.1: 16-20.

Kang, H. B., Jiang, J. W., Peng, J. C., et al. (2022). Simulation analysis on the initiation mechanism of the charge covered with a thick shell by rod-projectile impacts. Explosive and Shock Wave 42.1: 1-12.

LI, B., CHEN, X., Du, Z. H., et al. (2016). Numerical Simulation and Experimental Study of LEFP on Impact Initiation Process of Charge with Shell. J. Chinese Journal of Energetic Materials,24(11):1034-1040.

Guo, C., Zhang, X. F., Xiong, W. (2023) Cumulative Damage Effect on Shock Initiation of Covered Composition B by Dual EFP Impacts. Chinese Journal of Energetic Materials 31.8: 797-807.

Zhang, K., Zhao, C. X., Ji, C., et al. (2022). Numerical simulation and experimental study of the damage law of EFP warhead charging of cylindrical shells under different angles. Latin American Journal of Solids and Structures 19.4: e451.

Tarver, C. M., Chidester, S. K., Vandersall, K. S. (2018). Ignition and Growth Modeling of Shock Initiation of the TAB-based Explosives LX-17 and PBX 9502 at Eight Initial Temperatures Spanning a 446K Range. No. LLNL-PROC-753094. Lawrence Livermore National Lab. (LLNL), Livermore, CA (United States).

Zhang, A. Z., Li R. X., Xie, L. F., et al. (2025). Study on the penetration performance of shaped charge jet formed by nanocrystalline copper liner. Latin American Journal of Solids and Structures, 22(9), e8682.

Jia, X., Huang, Z. X., XU, M. W., et al. (2019). Theoretical Model and Numerical Study of Shaped Charge Jet Penetrating into Thick Moving Target. Acta Armamentarii, 40(8): 1553-1561.

Held, M. (1983). Critical area for the initiation of high explosive charges. Shock Waves in Condensed Matter. 555-557.

Li, R., Huang, Z. X., Zu, X. D., et al. (2018). Spallation of targets subjected to vertical penetration of explosively formed projectiles. J. Explosion And Shock Waves, 38(5): 1039-1044.

Tate, A. (1967). A theory for the deceleration of long rods after impact. Journal of the Mechanics and Physics of Solids 15.6: 387-399.

Alekseevskii, V. P. (1966). Penetration of a rod into a target at high velocity. Combustion, explosion and shock waves 2.2: 63-66.

Zhang, X. F. (2005). The study of shaped charge penetrator initiation of shelled charges. Nanjing University of Science and Technology.

Zhai, Y. X., Hao, W., Qin, F. (2017). Strength analysis of ceramic targets against hypervelocity penetration of long-rod projectiles based on A-T model. Journal of Vibration and Shock.

Held, M. (1989). Initiation phenomena with shaped charged jets. Proc of 9th Symp(int) on Detonation. Arington Va: OCNR.1416~1426.

Kim H. S., Arnold W., Hartmann T., et al. (2011). EFFECTS OF EFP SOLIDITY IN TERMINAL BALLISTICS. International Symposium on Ballistics.